3D fracture behaviours in dual-phase stainless steel

Toda, Hiroyuki
Department of Mechanical Engineering, 3D/4D Structural Materials Research Centre, Kyushu University

Tomizato, Fukuto
Department of Mechanical Engineering, Toyohashi University of Technology

Harasaki, Ryo
Department of Mechanical Engineering, Toyohashi University of Technology

Kobayashi, Masakazu
Department of Mechanical Engineering, Toyohashi University of Technology

他

出版情報：ISIJ International. 56 (5), pp.883-892, 2016-05-01
バージョン：
権利関係：

ISIJ International, Vol. 56 (2016), No. 5, pp. 883–892

3D Fracture Behaviours in Dual-phase Stainless Steel

Hiroyuki TODA,[1)]* Fukuto TOMIZATO,[2)] Ryo HARASAKI,[2)] Dowon SEO,[1)] Masakazu KOBAYASHI,[2)] Akihisa TAKEUCHI[3)] and Kentaro UESUGI[3)]

1) Department of Mechanical Engineering, 3D/4D Structural Materials Research Centre, Kyushu University, Motooka 744, Nishi-ward, Fukuoka City, Fukuoka, 819-0395 Japan. 2) Department of Mechanical Engineering, Toyohashi University of Technology, Hibarigaoka 1-1, Tempaku, Toyohashi, Aichi, 441-8580 Japan. 3) Japan Synchrotron Radiation Research Institute, Kouto 1-1-1, Sayo-cho, Sayo-gun, Hyogo, 679-5148 Japan.

(*Received on December 24, 2015; accepted on January 26, 2016*)

Single-distance phase retrieval technique was applied to contrast-enhanced phase-sensitive imaging of dual-phase microstructures in ferrite/austenite dual-phase stainless steel. Contrast between the two phases was evaluated, together with noise and spatial resolution, under varying experimental and phase retrieval conditions. Serial sectioning technique was also employed, to validate the shape accuracy of related three-dimensional images. Although the density difference between the two phases was relatively small, the two phases were successfully segmented in the three-dimensional images. The imaging technique was also applied to observe microvoid nucleation and growth behaviour during tensile loading. The loading steps at which microvoids were nucleated were identified by tracking all the microvoids observed at the final loading step, in reverse chronological order, toward the initial unloaded state. Each absorption-contrast image was then registered with a corresponding phase-contrast image, in order to classify all the targeted microvoids according to their nucleation site: ferrite, austenite or phase boundary. Premature damage initiation was observed at a relatively early stage at all the nucleation sites; however, subsequent growth was relatively moderate. On the other hand, microvoids initiated later, at fine particles located along the phase boundaries, exhibited enormous growth, thereby inducing the final rupture. It was concluded that the substantial driving force for the growth of microvoids located along morphologically characteristic austenitic particles was the predominant factor in the ductile fracture.

KEY WORDS: dual-phase material; stainless steel; microtomography; phase-contrast imaging; microvoid; ductile fracture.

1. Introduction

It is reasonable to assume that the ductile fracture process is more or less interrelated with underlying microstructure and texture, especially when the harder phases of a certain fraction are intricately intertwined with a softer matrix in three-dimension (hereinafter 3D). A good example of such characteristic damage behaviour is seen in dual-phase (DP) steels, which typically consist of a hard martensite phase, a soft ferritic phase, and small fractions of bainite and retained austenitic phases. However, in spite of extensive research activity aimed at elucidating the damage process in such DP steels, a variety of interpretations remain. For example, Ahmed *et al.*[1)] examined DP steels with a martensite volume fraction of 47–59%, and concluded that ferrite-martensite interfacial decohesion was the major mode of microvoid nucleation, while martensite cracking was less frequently observed. Avramovic-cingara *et al.*[2)] performed experiments whose results support a ferrite-martensite interfacial decohesion mechanism in the case of DP steels with 17% martensite volume fraction, while Kadkhodapour *et al.* reported microvoid nucleation due to ferrite grain-boundary decohesion in the neighbourhood of martensite particles when the martensite volume fraction was 23%.[3)] By contrast, Erdogan investigated DP microstructures with 18–26% martensite volume fraction, and concluded that coarse and interconnected martensite located along ferrite grain boundaries was the major damage nucleation site.[4)] It was also shown that ferrite-martensite interfacial decohesion became prominent when the fraction of new ferrite increased.[4)] Steinbrunner *et al.*[5)] reported martensite cracking as the major microvoid nucleation mechanism in the case of DP steels with a martensite volume fraction of 20%.

It appears that the differences in the reported damage micromechanisms may be partly attributed to different chemical compositions (especially carbon content) and/or thermo-mechanical histories. It should, however, be noted that each of the abovementioned studies employed SEM observation of the longitudinal sections of fractured tensile specimens, and behaviour identified in such a two-dimensional manner may often be surface-specific and unrepresentative of the bulk.[6)] This is because free-edge stress singularity is intense near grain boundaries and phase boundaries on the specimen surface, which results in accelerated decohesion along grain and phase boundaries.[7)] The 3D complexity of actual microstructures in practical materials, as partially illustrated by the close similarity among the SEM micrographs used

* Corresponding author: E-mail: toda@mech.kyushu-u.ac.jp
DOI: http://dx.doi.org/10.2355/isijinternational.ISIJINT-2015-631

as evidence in the abovementioned studies, also creates difficulty in determining governing mechanisms. It is therefore vital to apply robust 3D in-situ techniques in this area, in order to obtain conclusive evidence.

There have already been a number of attempts[8–13] to investigate microscopic damage mechanisms in DP steels by employing the recently improved high-resolution X-ray microtomography (hereinafter XMT) technique.[14] However, most of these studies have focused on simple damage evolution behaviour in continuum solids. Two-dimensional observation of longitudinal sections has been supplementarily employed for identifying microvoid nucleation mechanisms. Phase-contrast imaging techniques are capable of revealing DP microstructures, and enable the verification of microvoid nucleation sites. Landron *et al.* employed the holotomography technique to visualise the DP structure of a low-carbon DP steel with a 2.1% density difference between the martensitic and ferritic phases.[11] They succeeded in clearly distinguishing the two phases, but failed to observe the related damage evolution behaviour, due to the strong residual interference fringes that were induced by nucleated microvoids. The present authors have applied the single-distance phase retrieval technique to a ferrite/pearlite steel with only a 0.4% density difference between the two phases,[13] and have succeeded in distinguishing microvoids that were initiated, respectively, in the ferrite or pearlite phases, or at phase boundaries. However, in spite of such recent investigations into the ductile fracture of DP steels, using state-of-the-art imaging techniques, the detailed damage process has yet to be fully understood.

In this work, the damage initiation and growth behaviour of a DP steel has been investigated using the phase-contrast XMT technique. A combination of the microstructural tracking technique[15] and the phase-sensitive imaging technique have enabled damage evolution behaviour such as the identification of microvoid nucleation sites and subsequent growth behaviour, together with damage micro mechanisms. A ferrite/austenite DP stainless steel, with little difference in density or deformation resistance between the two phases, has been chosen for evaluation and demonstration purposes, instead of the usual, ferrite/martensite DP steels.

2. Experimental

2.1. Material Used

A commercial super duplex stainless steel, Sandvik SAF2507, with a chemical composition of 25.30 Cr, 6.57 Ni, 4.18 Mo, 0.92 Mn, 0.39 Si, and balance iron in mass%, was used in this study. SAF2507 has a DP structure consisting of ferritic and austenitic phases. The average volume equivalent diameter (*i.e.*, the diameter of a sphere with volume equal to that of a non-spherical particle) and volume fraction of austenitic particles were 33.4 μm and 51.8%, respectively. An as-received material was solution-annealed at 1 398 K, followed by quenching, and then stress-relieved at 623 K for 18 ks. The austenitic phase had a slightly lower micro-Vickers hardness value (HV265) than the ferritic phase (HV276) before loading, but was 18% harder after fracture (HV397 vs. HV336). A small parallel-piped specimen, with nominal dimensions of about 600 × 600 μm^2 in the gauge section and about 400 μm in gauge length, was sampled in parallel to the rolling direction using an electro discharge machining apparatus. Detailed specimen geometry is available elsewhere.[16]

2.2. 3D Imaging

The XMT experiments were performed using an undulator beamline (BL20XU) of SPring-8. A monochromatic X-ray beam of 37.7 keV was produced by a liquid nitrogen-cooled Si (111) double crystal monochromator. A material test rig specially designed for in-situ mechanical tests at synchrotron radiation facilities was positioned approximately 240 m from the X-ray source. The sample-to-detector distance was 65 mm for the absorption-contrast XMT, and was varied between 8 and 1 200 mm for the phase-contrast XMT. A CMOS camera (ORCA Flush 4.0, Hamamatsu Photonics K. K.) of 4.0 megapixels, with a 10 μm thick Lu_2SiO_5:Ce scintillator, was used for acquiring projection images. The stress - strain curve obtained during the tensile test performed at a loading rate of 0.0005 mm/sec is shown in **Fig. 1**. Both the absorption-contrast and phase-contrast XMT scans were repeated 11 times before fracture, while maintaining displacement.

A total of 1 800 and 3 600 radiographs, scanning 180°, were obtained in each absorption-contrast and phase-contrast XMT scan, respectively. A propagation-based single-distance phase retrieval algorithm using Paganin's method was applied, to reconstruct a projected distribution of linear attenuation coefficients from a single projection image per projection.[17–19] Noise, spatial resolution, and contrast between the two phases were quantitatively evaluated in the reconstructed slices, in order to optimise imaging and phase retrieval conditions, such as propagation distance, X-ray energy, and parameters for the phase retrieval process. A conventional filtered backprojection algorithm was employed to reconstruct image slices for both the absorption-contrast and phase-contrast images. Isotropic voxels with 0.5 μm edges were achieved in both the reconstructed slices.

To employ the phase retrieval algorithm in the case of DP materials, a priori knowledge of δ_i and β_i (*i.e.*, the refractive index and extinction coefficient in the complex refractive index for the *i*th phase), as well as the total projected thickness of the sample, are required. In order to accurately

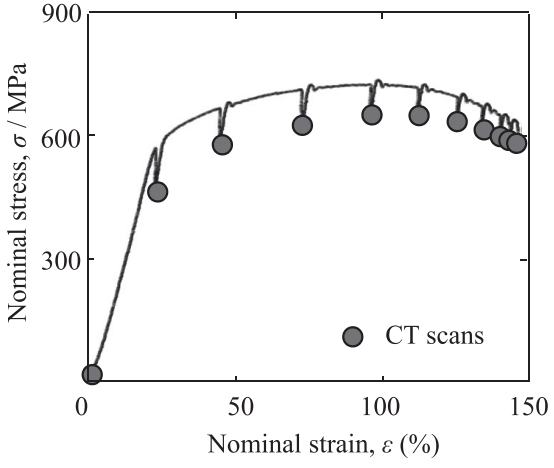

Fig. 1. Nominal stress - nominal strain curve for an in-situ tensile test.

determine the in-situ densities of the ferritic and austenitic phases, XRD measurements were performed before loading, by replacing only the CMOS camera with a large-area flat-panel detector with a field of view of 44.80 mm × 47.36 mm (2 240 pixels × 2 368 pixels, C7942-CA, Hamamatsu Photonics K. K.).

2.3. Image Analyses

2.3.1. 3D Volume Rendering and Qualitative Image Analysis

The linear absorption coefficient values for the ferritic and austenitic phases are roughly 33.5–34.5 cm^{-1} at an X-ray energy of 37.7 keV. The grey value in the XMT images was calibrated such that the linear absorption coefficients from −6 to 41 cm^{-1} fell within an 8-bit grey-scale range. To estimate the volume of individual microvoids and particles with sub-voxel accuracy, facetted iso-intensity surfaces of pentagonal shape were computed on the basis of the Marching Cubes algorithm. To suppress inaccuracies originating from image noise, only features over 23.168 voxels in volume were counted as particles and microvoids in the XMT images.

The specimen was then sectioned using a focussed ion beam (hereinafter FIB) apparatus, to identify specific particles corresponding to those observed in the 3D XMT image. A total of eight particles were analysed. According to SEM-EDX analysis of the particles, they were complex oxides bearing Al–Ca or Al–Mg. Segregation of Mo or Ti was sometimes observed in part of the particles.

The modulation transfer function (MTF), derived from the edge response function[20] at the ferrite/austenite interfaces, was measured, in order to determine the spatial resolution at a 5% contrast ratio in the phase-contrast XMT images. It has been reported by the present authors that the results of interface-based MTF calculations and those obtained with 3D test patterns showed reasonable agreement.[12] Noise was also measured in the phase-contrast images, by calculating the standard deviation inside given regions of interest (30 pixels × 30 pixels × 5 regions) for each image. In order to evaluate the efficiency of the single-distance phase retrieval technique, contrast was defined by substituting average grey values between the ferritic and austenitic phases.

2.3.2. Microvoid Analysis

Microvoids were tracked in reverse chronological order, from the last loading step (shown in Fig. 1) towards the initial unloaded state, by employing the microstructural tracking method.[15,21] As mentioned earlier, particles have linear absorption coefficients similar to microvoids and pre-existing pores. It is therefore difficult to distinguish

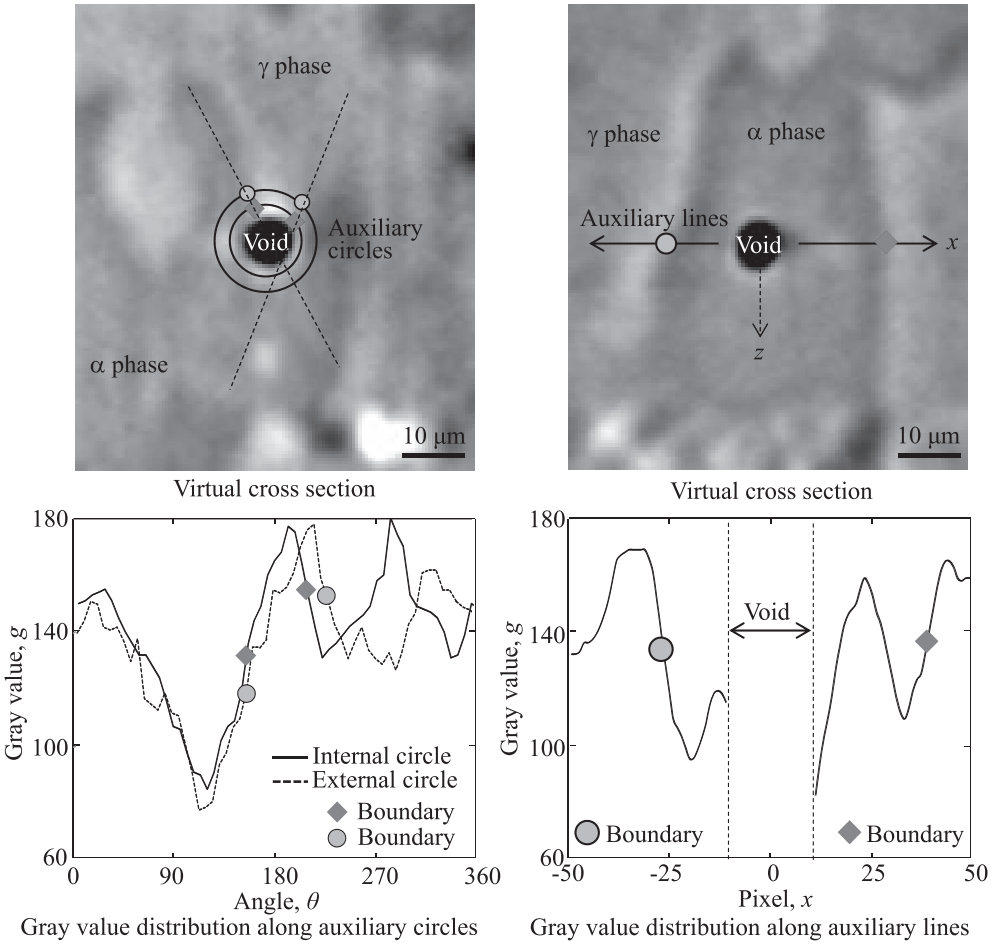

Fig. 2. Examples of void location determination. Voids are classified as (a) interfacial voids when auxiliary lines that connect two boundary locations detected by inner and outer circles pass through the void in question. The remaining voids (b) are then examined, to determine whether they are located in the α or γ phase.

between pre-existing pores and particles, and also difficult to detect microvoid nucleation during the reverse tracking process when microvoids are nucleated from visible particles (*i.e.*, particles larger than the 1 μm spatial resolution of the absorption-contrast XMT images). In response to these difficulties, the criterion for microvoid nucleation was determined to be 1.71 in volume ratio with respect to the initial unloaded state.

Since the density difference between the ferritic and austenitic phases is too small to accurately segment the two phases, it was difficult to identify the nucleation sites of some of the microvoids. Thus, intensity distribution associated with Fresnel diffraction around microvoids was here utilised for analysis of nucleation sites, as shown in **Fig. 2**(a). Two auxiliary circles were drawn on a virtual cross section passing through the gravity centre of a given microvoid. An interface was detected when the grey value showed abrupt changes. When all the lines connecting two points that intersected both circles penetrated the microvoid, as shown in Fig. 2(a), the latter was classified as a microvoid located at the interface. Otherwise, intensity distribution associated with Fresnel diffraction at the ferrite/austenite interfaces was utilised, to determine if the microvoid was located in ferrite or austenite, as shown in Fig. 2(b).

3. Observation of DP Structure

It has been reported for SAF2507 that the chemical compositions of ferrite and austenite are 26.65Cr-5.45Ni-4.56Mo-2.05Mn-0.58Si, and 23.55Cr-7.92Ni-2.94Mo-1.71Mn-0.50Si,[21] yielding linear absorption coefficients of 34.5/cm and 33.9/cm, respectively. This implies that absorption-contrast imaging would be completely unable to distinguish the two phases. Lattice constant values averaged over the seven crystal planes for ferrite and austenite were 0.2890 nm and 0.3629 nm, respectively; and the density values were accordingly calculated as 7.65 g/cm^3 and 7.71 g/cm^3 for the ferrite and austenitic phases, respectively, implying a relatively small density difference of 0.8%.

Figure 3 shows an identical virtual cross-section captured at different sample-to-detector distances. It appears that the contrast between the two phases is gradually enhanced with the increase in sample-to-detector distance together with the improvement in signal-to-noise ratio. The absorption-contrast image shown in Fig. 3(a) would appear to represent the DP structure. It is, however, to be noted that only the interfaces are highlighted (with pairs of black and white fringes), and the grey levels in the interiors of the two phases are similar. In Fig. 3(b), the phase-retrieved images appear very noisy. It has been reported that in a relatively high X-ray energy range, preferential forward scattering occurs,[12,14] which results in a remarkably low signal-to-noise ratio and spatial resolution when the sample-to-detector distance is less than 50 mm.[12,14] On the other hand, the ring artefacts observed above a sample-to-detector distance of 50 mm are gradually annihilated in the long-distance images. This may be attributable to degradation in the spatial resolution. The image of the microvoid (shown in black) located slightly to the upper right of centre in Figs. 3(a)–3(d) is clearly enlarged with the increase in sample-to-detector distance. This is due both to X-ray divergence of the order of a few μrad, and to X-ray deflection, implying loss in quantitative size capability in the phase-retrieved images.

Figure 4 shows the results of quantitative evaluation of the phase-retrieved images. The signal-to-noise ratio is almost constant when the sample-to-detector distance is greater than 400 mm. Contrast is enhanced almost linearly with the increase in sample-to-detector distance, while spatial resolution is *per contra* degraded. The sample-to-detector distance value for the subsequent microvoid analyses was determined to be 400 mm, where a combination of reasonable contrast and superior spatial resolution was

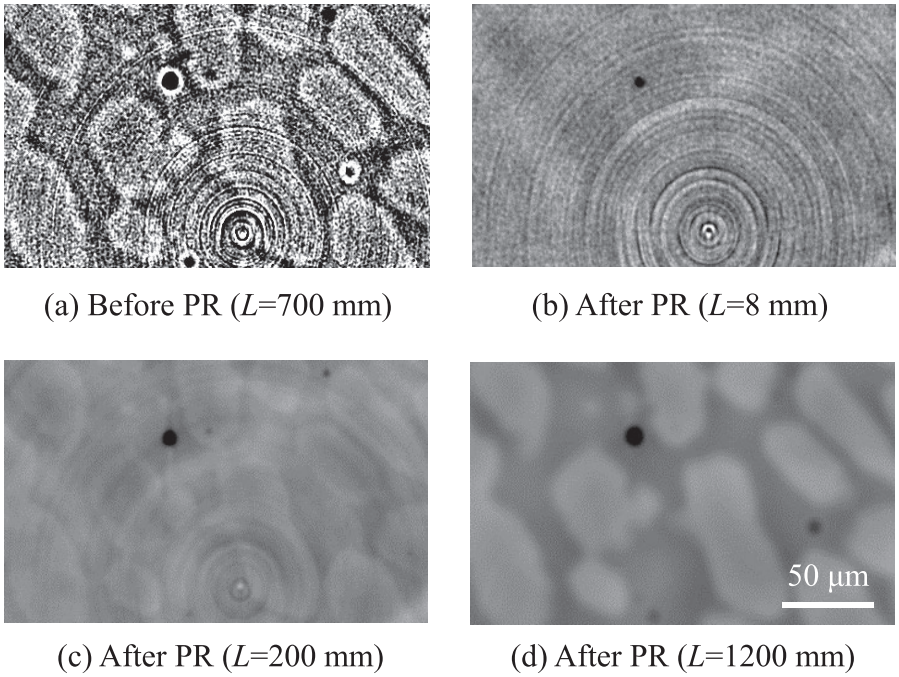

(a) Before PR (L=700 mm) (b) After PR (L=8 mm)

(c) After PR (L=200 mm) (d) After PR (L=1200 mm)

Fig. 3. 3D images before and after phase retrieval (PR), shown as a virtual cross section. Sample-to-detector distance, L, was varied between 8 and 1 200 mm for the phase-retrieved images.

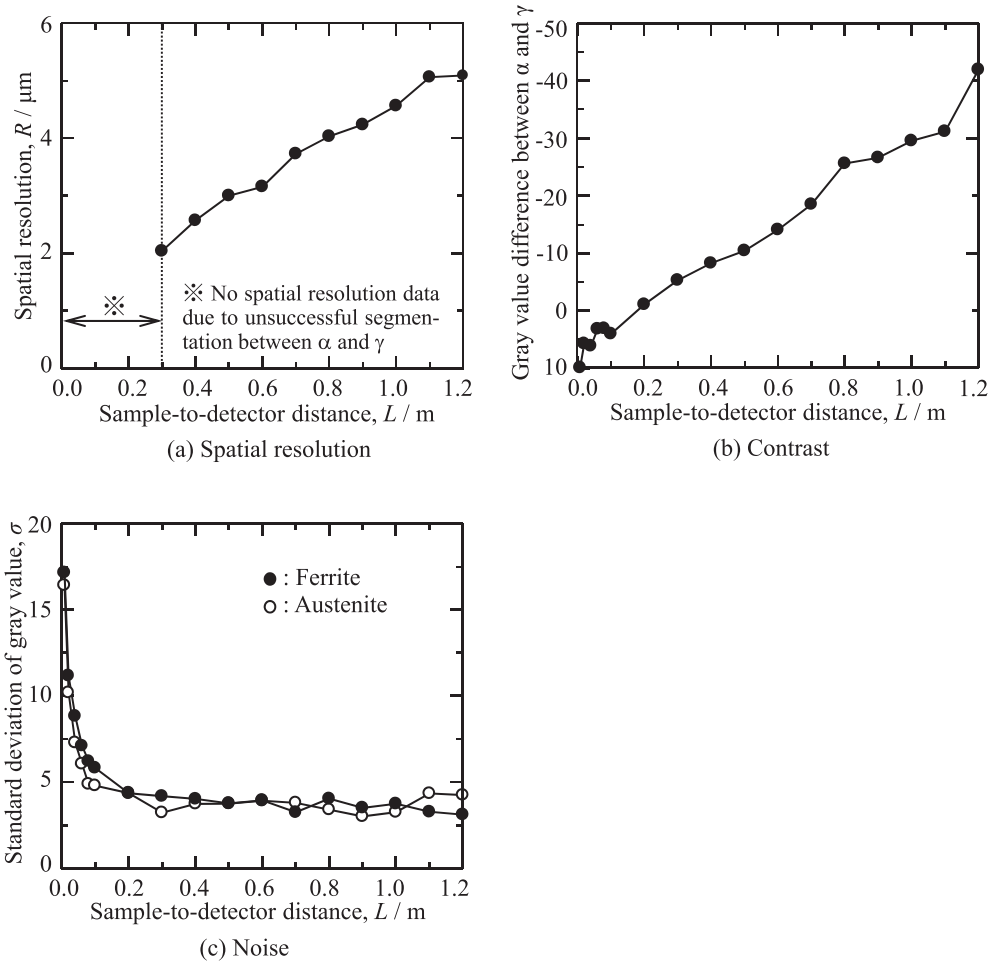

Fig. 4. Changes in (a) spatial resolution, (b) contrast, and (c) noise, as a function of sample-to-detector distance. Spatial resolution was measured as the FWHM of differential grey value transition at the α/γ interfaces. The grey value difference between the α and γ phases, and the standard deviation in grey value, were used for evaluating contrast and noise, respectively.

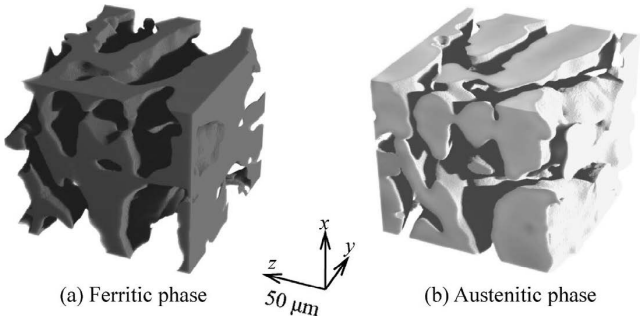

Fig. 5. 3D volume-rendered images of the (a) ferritic phase and (b) austenitic phase after phase retrieval.

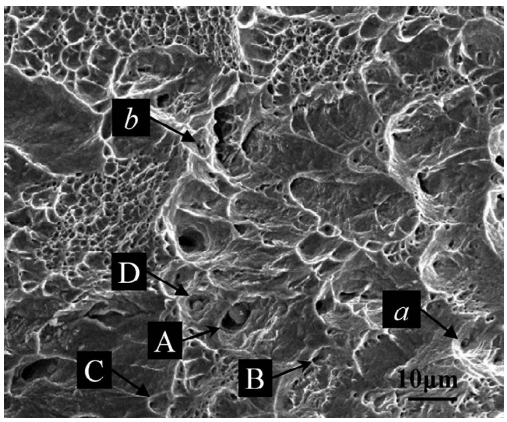

Fig. 6. SEM fractographs of the specimen. Marks A–D show the dimples.

available, together with a high signal-to-noise ratio.

Figure 5 shows the optimised 3D images. Both of the phases are clearly distinguished and the microstructural features, such as particles and pores, are readily identified at interfaces, as shown in Figs. 5(a) and 5(b). Overall, the DP structure can be successfully visualised after the phase retrieval process, unlike in the case of the absorption-contrast image (Fig. 3(a)).

4. Damage Evolution Behaviour

Figure 6 shows SEM fractographs of the fracture surfaces of the specimen that was fractured in-situ in the XMT experiment. Dimples A–D are observed on the fracture surfaces. Clearly, particles are observable at the dimple patterns, implying that these microvoids were nucleated according to particle/matrix interfacial debonding. It is also observable that these primary voids are more or less elongated due to shear deformation. In contrast to the primary dimples, which are typically 5 μm to 13 μm in diameter, part of the fracture surface is covered with small secondary dimples that

appear relatively equiaxed compared to the primary voids. The particles that can be seen at the dimples typically range between 3 μm and 5 μm in projected diameter, implying that these particles would be observable using the XMT technique of the present study. However, particles smaller than 1 μm, such as those indicated as *a* and *b* in Fig. 6, are sometimes observed at the primary microvoids.

Figure 7 shows a series of 3D perspective views of microvoids at selected applied-load levels. Microstructural features segmented with a threshold X-ray linear absorption coefficient of 100 in grey value, determined according to the preliminary investigation in Section 2.3.1, are displayed, without displaying the underlying ferritic and austenitic phases. The microstructural features shown are mainly

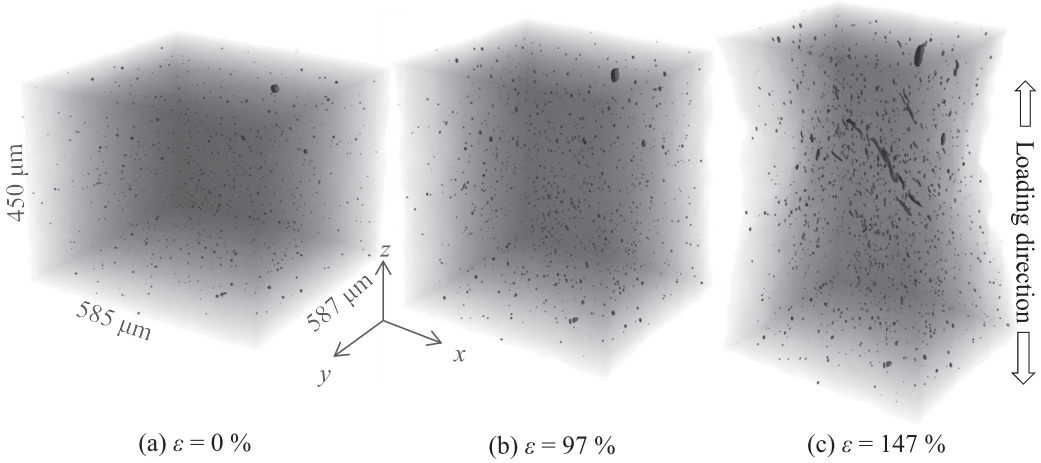

Fig. 7. 3D perspective views of particles and microvoids at different load levels.

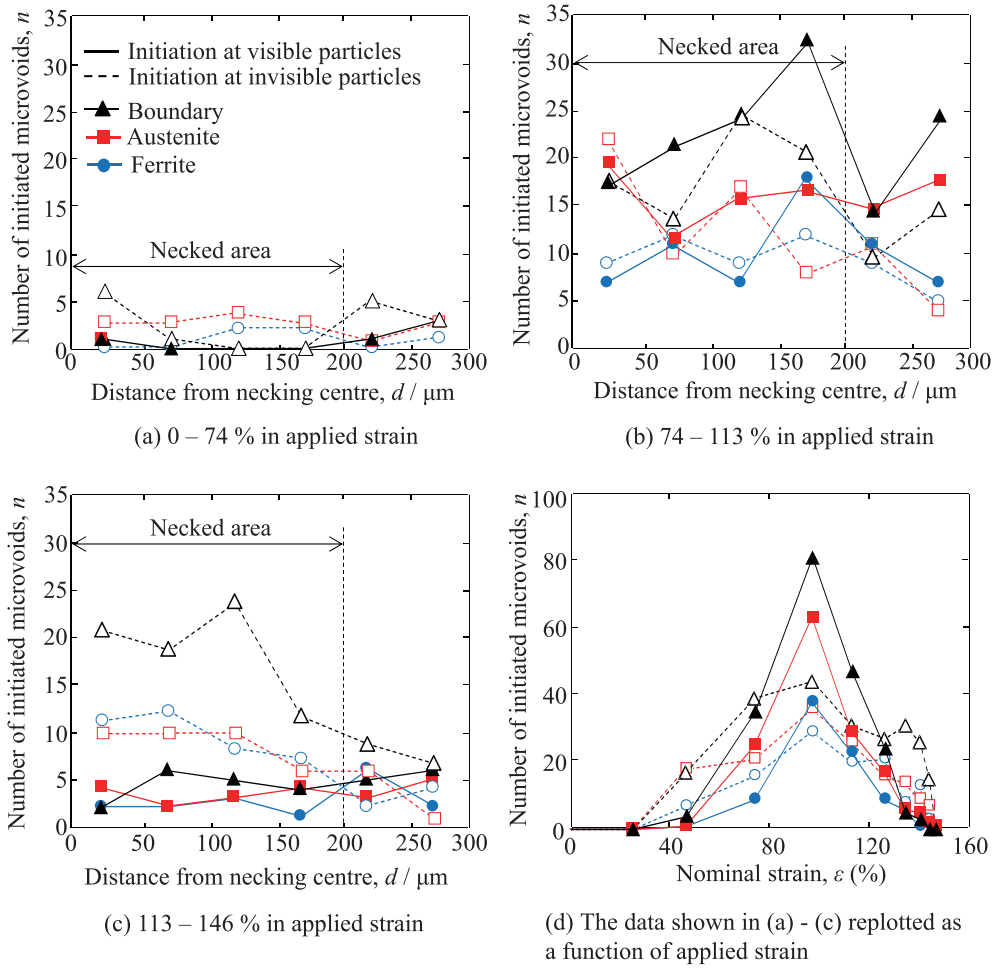

Fig. 8. Number of initiated microvoids at different applied strain levels, as a function of distance from the necking centre: (a) uniform elongation regime, (b) vicinity of the maximum load, and (c) localized deformation. The data were organised according to the microvoid initiation sites and the size of particles that caused particle damage (*i.e.*, smaller or larger than the spatial resolution level of the present microtomography setup). (Online version in color.)

microvoids, but may contain some pre-existing particles. Figs. 7(b) and 7(c) correspond to the maximum load and the final loading step immediately before fracture, respectively. In comparison with Fig. 7(a), clear increases in the number density and volume fraction of microvoids are observed in Fig. 7(b). This indicates that the growth of pre-existing pores occurs together with relatively uniform nucleation of new microvoids, even during the uniform elongation of the specimen. Extremely coarse microvoids are observed in Fig. 7(c), especially where necking has occurred. It is interesting to note that the majority of such coarse microvoids were significantly elongated and aligned in the oblique directions.

In **Fig. 8**, all the microvoids that were observed at the final loading step have been tracked, in reverse chronological order, to identify the loading step at which each microvoid was initiated. All the microvoids have been classified according to their nucleation site (*i.e.*, ferrite interior, austenite interior, or ferrite/austenite interface), their distance from the centre of necking in the tensile direction, and the size of the particle from which they were nucleated. In addition, they have been classified into two size levels defined: visible or invisible, with approximately 1 μm (*i.e.*, the spatial resolution of the present technique) as the threshold. The loading steps at which microvoids were initiated were divided into three regimes: uniform deformation (0–0.74 in applied strain), vicinity of the maximum load (0.74–1.13 in applied strain), and localised deformation (1.13–1.46 in applied strain). Noteworthy is the presence, throughout deformation, of a large number of microvoids initiated from finer particles that are below the spatial resolution of the present set-up (Fig. 8). During the uniform deformation shown in Fig. 8(a), microvoid nucleation is unusually dormant, except for some limited nucleation from fine particles located at ferrite/austenite interfaces. Interfacial damage nucleation is later activated around the maximum load (Fig. 8(b)), especially at coarse particles. Coarse particles located in the interior of austenite, and to a lesser extent in the interior of ferrite, are also damaged around the maximum load, probably due to the relatively high strain hardenability of the austenitic phase compared to the ferritic phase. Damage nucleation at coarse particles is not extensively observed after applied strain of 1.34, as shown in Figs. 8(c) and 8(d), whereas microvoid nucleation at fine particles located at ferrite/austenite interfaces still remains active in the necked area during localised deformation.

The overall microvoid growth behaviour is summarised in **Fig. 9**. The magnitude relation in the simple arithmetic mean in microvoid size, between coarse and fine particles, is mostly maintained throughout deformation (Fig. 9(a)). However, in terms of volume fraction (Fig. 9(b)), the microvoids nucleated at fine particles rapidly approach those nucleated at coarse particles, with increasing nominal strain. This may suggest the existence of a limited number of extremely coarse microvoids, and/or extensive nucleation without significant growth in the case of microvoids nucleated from fine particles.

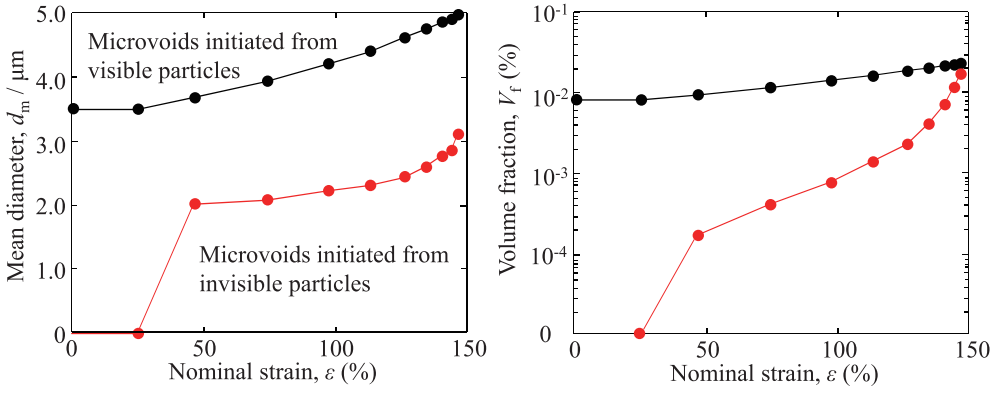

Fig. 9. Change in mean diameter and volume fraction of microvoids. (Online version in color.)

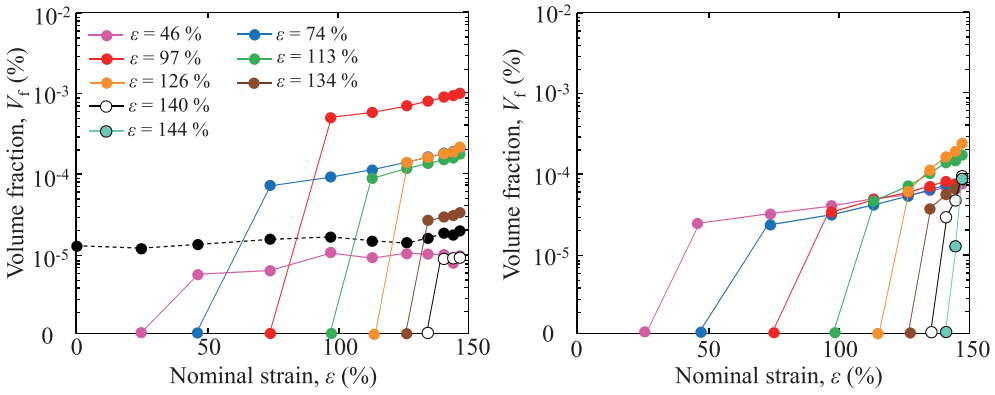

Fig. 10. Growth behaviour of microvoids initiated at different applied strain levels. The data for microvoids located within 50 μm of the necking centre is shown. (Online version in color.)

The data in Fig. 9 has been analysed according to the loading steps at which microvoids were initiated, as shown in **Fig. 10**. It is interesting to note that microvoids nucleated later, which are in many cases located at the ferrite/austenite interfaces, tend to grow rapidly compared to those nucleated earlier. The maximum growth rate for nucleated microvoids is observed at an applied strain of 0.97 in the case of coarse particles (Fig. 10(a)), and 1.26 in the case of fine particles (Fig. 10(b)).

This tendency is confirmed in **Fig. 11**, where microvoid nucleation and growth behaviour within the necked area shown in Fig. 7(c) are revealed in magnified images. The majority of the coarse particles (highlighted in light blue) are damaged before the maximum load, and no coarse particles remain intact at an applied strain of 1.26. The eight microvoids with high aspect ratios (indicated by arrows in Fig. 11(e)) were nucleated at the ferrite/austenite interfaces at an applied strain of 1.26 or later. Such microvoids are more or less oriented obliquely with respect to the loading direction, and exhibit remarkably high growth rates. The largest microvoid (A in Fig. 11(e)) has been extracted in **Fig. 12**, together with adjacent austenitic particles. Microvoid A was nucleated at an applied strain of 1.26, at the interface between a slender austenitic particle and a thin oblong ferritic film. The ferritic film was sandwiched between two obliquely oriented austenitic particles, and is viewed in the x direction in Fig. 12. Microvoid A was nucleated at a few separate nucleation sites along the same austenitic particle, and these individual microvoids coalesced, between an applied strain of 1.40 and 1.46, to form the thin oval-shaped microvoid shown in Fig. 12.

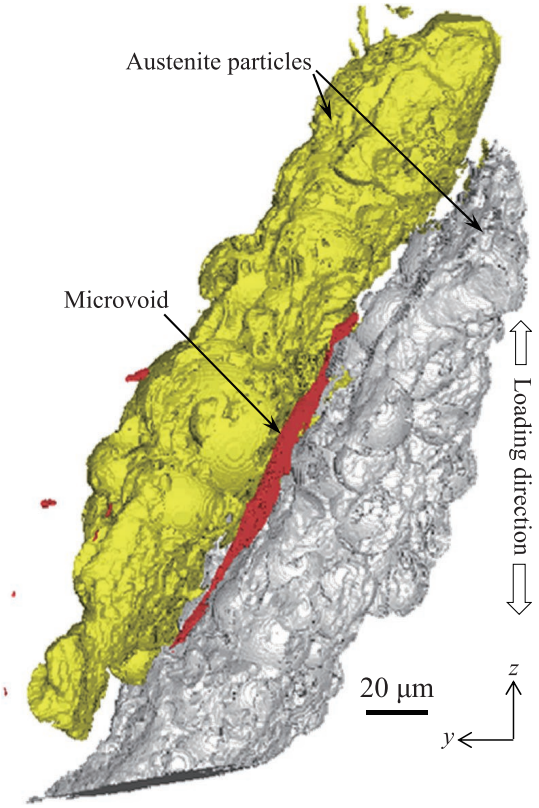

Fig. 12. 3D perspective view of the coarsest microvoid (highlighted in red) shown in Fig. 11, which exhibited rapid growth after the maximum load. The void was initiated at an applied strain of 1.26, from an invisible particle located between slender aligned austenitic particles (highlighted in grey and yellow). (Online version in color.)

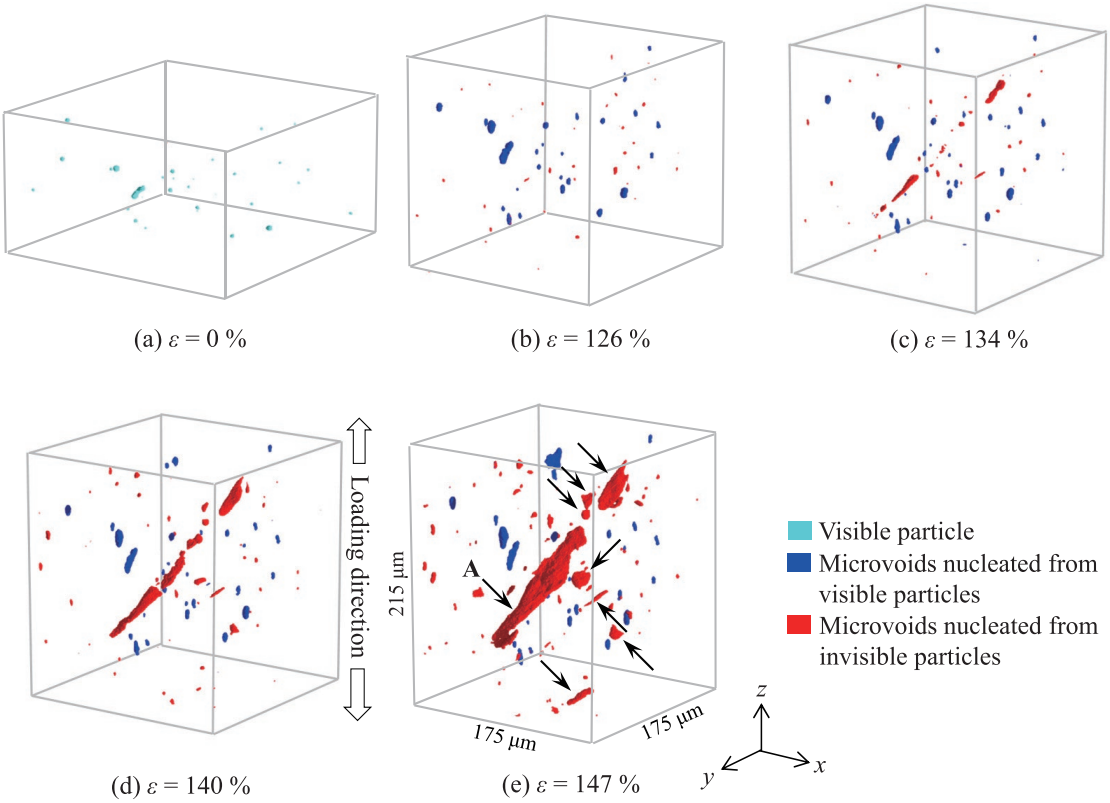

Fig. 11. Magnified 3D perspective views of microvoid initiation and growth behaviour in part of the tensile specimen. Different colours indicate different particle sizes for microvoid nucleation. (Online version in color.)

5. Discussion

It has been generally believed that microvoid nucleation is proportionally dependent on equivalent plastic strain, that microvoid growth is governed by stress triaxiality, and that microvoid coalescence is controlled by the maximum shear stress through the void-sheet mechanism.[22] It has been well documented that the in-situ fracture strength of particles increases with decreasing particle size.[23] One of the striking results obtained in the present image-based analyses was that damage evolution appeared to be controlled by growth and coalescence processes in the DP stainless steel investigated. It can be therefore inferred that, at least in this case, microstructural controls, such as reduction in particle size and/or particle volume fraction, may have less influence in controlling mechanical properties.

Microvoid growth has been phenomenologically postulated according to the existence and degree of triaxial stress state.[24] In general, the triaxial driving force for microvoid growth has been assumed to arise due to the formation of a macroscopic neck under tension.[25] However, in the present study, the microvoid growth observed before the onset of necking (Figs. 9 and 10) is not explained by this mechanism. Another possible source for the early elevation in stress triaxiality would be plastic constraint due to the interaction between dissimilar phases. It can be inferred that the relatively weak interaction between the two phases, which exhibited similar hardness values at the initial unloaded state, does not induce microvoid growth before the onset of necking.

Although the number of particles located on ferrite/austenite boundaries seemed remarkably limited, the damage evolution on such boundaries predominated over that which occurred in the interior of the ferritic and austenitic phases. Enormous growth of limited microvoids was observed at the ferrite/pearlite boundaries, especially in the case of microvoids nucleated at finer particles after maximum load was reached. This implies that the finer particles were sampled as a result of intense strain localisation, and that the driving forces for subsequent growth and coalescence were a controlling factor. The most likely explanation for the rapid microvoid growth along the borders of obliquely aligned austenitic particles lies in intense strain localisation on phase boundaries; and the differences noted between this stage and the uniform elongation regime may be explained by enhanced deformation resistance in the austenitic phase due to high strain hardening, as discussed in Section 2.1.

The rapid growth observed in the case of the interfacial microvoids cannot be explained simply by the development of macroscopic stress triaxiality. It has recently been recognised that the well-known Gurson-type models are unable to model ductile fracture under shear-dominated stress states.[26] It is well known that, in addition to remote mixed-mode loading conditions, the void-sheet mechanism involves microvoid growth in a shear band inclined toward a loading direction, even in tensile tests.[27] This would appear to bear some affinity with the propagation of microvoids through the very narrow ferritic channels in the present study, as shown in Fig. 12. Nahshon and Hutchinson have extended the Gurson-type model to cover low-triaxiality shear-dominated states.[28] The microvoid growth rate, $\dot{f}$, is expressed in their model as follows:

$$\dot{f} = (1-f)\dot{\varepsilon}^p_{kk} + k_\omega f \omega \frac{s_{ij}\dot{\varepsilon}^p_{ij}}{\sigma_e}, \quad \text{..... (1)}$$

where f is the microvoid volume fraction, $\dot{\varepsilon}^p_{kk}$ the rate of plastic volume change, k_ω a constant expressing the magnitude of the damage growth rate in shear, ω the deviatoric stress state parameter, s_{ij} the stress deviator, $\dot{\varepsilon}^p_{ij}$ the plastic strain rate, and σ_e the effective stress. If a pure shear state (*i.e.*, $\omega = 1$) is assumed, Eq. (1) becomes:

$$\dot{f} = k_\omega f \dot{\gamma}^p_{kk} / \sqrt{3}, \quad \text{..... (2)}$$

where $\dot{\gamma}^p_{kk}$ is the plastic shear strain rate. Xue *et al.* obtained a k_ω value of 1.1 for a Weldox 420 fine-grained steel, which has a yield stress value (σ_y = 415 MPa) similar to that of the present DP stainless steel.[29] Making the bold assumption that the contribution from triaxial tension is negligible, $\dot{\gamma}^p_{kk}$ is here estimated to be 1.48, 1.22, 0.94 and 0.76 for the 7th-8th, 8th-9th, 9th-10th and 10th-11th loading steps, respectively, using the above k_ω value and the measured f and $\dot{f}$ values for Microvoid A. Considering that the values for shear strain to fracture, reported for mild steels, range from 0.5 to 0.85,[30] these estimated local plastic shear strain rate values seem high enough to locally expand the microvoid within a short period of time. The highest $\dot{\gamma}^p_{kk}$ calculated for the 7th-8th loading steps corresponds to the fastest microvoid growth rate shown in Fig. 10(b). It can be also explained partly with the enlarged difference in deformation resistance between the two phases due to the high strain hardening of the austenitic phase.

Finally, it is noteworthy that the gradual increase in deformation mismatch between the ferritic and austenitic phases is fundamentally attributable to the accelerated growth of microvoids initiated at the ferrite/austenite interfaces. This implies that control of the spatial distribution of the austenitic phase is of crucial importance to the improvement of mechanical properties attainable through control of the damage evolution process. On the other hand, conventional microstructural controls, such as reduction in particle size and/or particle volume fraction, might not be of great significance at least in the case of the DP stainless steel investigated.

6. Summary

High-resolution XMT has been applied to DP stainless steel. The single-distance phase retrieval technique has been successfully employed to visualise, in 3D, ferrite/austenite DP structure with relatively small density difference. Although spatial resolution is more or less degraded during the phase retrieval process, contrast, noise and spatial resolution have been optimised for the DP stainless steel used. Microvoid nucleation, growth and coalescence behaviour have been investigated, by tracking all the microvoids observed at the final loading step, in reverse chronological order, from the final loading state towards the initial unloaded state, in high-resolution absorption-contrast images. A combination of high-contrast phase-contrast images and high-resolution absorption-contrast images has enabled both observation and quantitative analysis of

microstructure/damage evolution relationships under tension in order to classify all the targeted microvoids according to their nucleation site: ferrite, austenite or phase boundary.

Premature damage initiation was observed at a relatively early stage at all the nucleation sites; however, subsequent growth was relatively moderate. For example, coarse particles located in the interior of austenite, and to a lesser extent in the interior of ferrite, are damaged.

Microvoids initiated from particle/matrix interfacial debonding of particles smaller than 1 μm were nucleated throughout most of the deformation period, while particles coarser than 1 μm (*i.e.* those observable using the XMT technique of the present study), which typically range 3 μm and 5 μm in projected diameter, were intensively damaged due to particle/matrix interfacial debonding around the maximum load. A limited number of microvoids initiated during macroscopic necking at fine particles located on ferrite/austenite boundaries exhibited enormous growth, thereby inducing macroscopic ductile fracture. This was attributable to the high driving force for microvoid growth, acting on such a limited number of extremely coarse microvoids, which were located at morphologically specific ferrite/austenite boundaries (*i.e.*, more or less oriented obliquely with respect to the loading direction, especially where a thin oblong ferritic film intervenes between slender austenitic particles). This implies that the finer particles were statistically sampled as a result of intense strain localisation on phase boundaries, and that the driving forces for subsequent growth of microvoids through the very narrow ferritic channels were a controlling factor for ductile fracture under local shear-dominated stress states.

Acknowledgements

The synchrotron experiments were performed with the approval of JASRI, through proposal numbers 2012B1595 and 2012B1629. This study was undertaken with the support of the ISIJ Innovative Program for Advanced Technology from the Iron and Steel Institute of Japan, through the subject entitled “Breakthrough in research on steel by realizing 4D imaging”.

REFERENCES

1) E. Ahmad, T. Manzoor, M. M. A. Ziai and N. Hussain: *J. Mater. Eng. Perform.*, **21** (2012), 382.
2) G. Avramovic-Cingara, Ch. A. R. Saleh, M. K. Jain and D. S. Wilkinson: *Metall. Mater. Trans. A*, **40** (2009), 3117.
3) J. Kadkhodapour, A. Butz and S. Ziaei Rad: *Acta Mater.*, **59** (2011), 2575.
4) M. Erdogan: *J. Mater. Sci.*, **37** (2002), 3623.
5) D. L. Steinbrunner, D. K. Matlock and G. Krauss: *Metall. Trans. A*, **19** (1988), 579.
6) J.-Y. Buffiere, E. Maire, P. Cloetens, G. Lormand and R. Fougeres: *Acta Mater.*, **47** (1999), 1613.
7) V. L. Hein and F. Erdogan: *Int. J. Fract. Mech.*, **7** (1971), 317.
8) E. Maire, O. Bouaziz, M. D. Michiel and C. Verdu: *Acta Mater.*, **56** (2008), 4954.
9) C. Landron, O. Bouaziz, E. Maire and J. Adrien: *Scr. Mater.*, **63** (2010), 973.
10) C. Landron, E. Maire, O. Bouaziz, J. Adrien, L. Lecarme and A. Bareggi: *Acta Mater.*, **59** (2011), 7564.
11) C. Landron, E. Maire, J. Adrien, H. Suhonen, P. Cloetens and O. Bouaziz: *Scr. Mater.*, **66** (2012), 1077.
12) H. Toda, F. Tomizato, F. Zeismann, Y. Motoyashiki-Besel, K. Uesugi, A. Takeuchi, Y. Suzuki, M. Kobayashi and A. Bruckner-Foit: *ISIJ Int.*, **52** (2012), 516.
13) H. Toda, A. Hosokawa, D. Seo and M. Kobayashi: Proc. 4th Int. Symp. Steel Science (ISSS2014), ISIJ, Tokyo, (2014), O08.
14) D. Seo, F. Tomizato, H. Toda, K. Uesugi, A. Takeuchi, Y. Suzuki and M. Kobayashi: *Appl. Phys. Lett.*, **101** (2012), 261901.
15) M. Kobayashi, H. Toda, Y. Kawai, T. Ohgaki, K. Uesugi, D. S. Wilkinson, T. Kobayashi, Y. Aoki and M. Nakazawa: *Acta Mater.*, **56** (2008), 2167.
16) H. Toda, H. Oogo, K. Uesugi and M. Kobayashi: *Mater. Trans.*, **50** (2009), 2285.
17) D. Paganin, S. C. Mayo, T. E. Gureyev, P. R. Miller and S. W. Wilkins: *J. Microsc.*, **206** (2002), 33.
18) M. A. Beltran, D. M. Paganin, K. Uesugi and M. J. Kitchen: *Opt. Express*, **18** (2010), 6423.
19) S. C. Mayo, A. W. Stevenson and S. W. Wilkins: *Materials*, **5** (2012), 937.
20) I. A. Cunningham and A. Fenster: *Med. Phys.*, **14** (1987), 533.
21) H. Toda, E. Maire, Y. Aoki and M. Kobayashi: *J. Strain Anal. Eng. Des.*, **46** (2011), 549.
22) Y. Lou, H. Huh, S. Lim and K. Pack: *Int. J. Solids Struct.*, **49** (2012), 3605.
23) H. Toda, T. Kobayashi, A. Hoshiyama and A. Takahashi: *J. Jpn. Inst. Met.*, **51** (2001), 113.
24) J. R. Rice and D. M. Tracey: *J. Mech. Phys. Solids*, **35** (1969), 201.
25) R. D. Thomson and J. W. Hancock: *Int. J. Fract.*, **26** (1984), 99.
26) Y. Bao and T. Wierzbicki: *Int. J. Mech. Sci.*, **46** (2004), 81.
27) J. P. Bandstra, D. M. Goto and D. A. Koss: *Mat. Sci. Eng. A*, **249** (1998), 46.
28) K. Nahshon and J. W. Hutchinson: *Eur. J. Mech. A/Solid*, **27** (2008), 1.
29) Z. Xue, J. Faleskog and J. W. Hutchinson: *Int. J. Solids Struct.*, **50** (2013), 4258.
30) I. E. French and P. F. Weinrich: *Metall. Trans. A*, **10** (1979), 297.